JACS
JOURNAL OF THE AMERICAN CHEMICAL SOCIETY
pubs.acs.org/JACS
Article

Unraveling the Structural Sensitivity of CO_2 Electroreduction at Facet-Defined Nanocrystals via Correlative Single-Entity and Macroelectrode Measurements

Soojin Jeong,[#] Myung-Hoon Choi,[#] Gargi S. Jagdale, Yaxu Zhong, Natasha P. Siepser, Yi Wang, Xun Zhan, Lane A. Baker,* and Xingchen Ye*

Cite This: *J. Am. Chem. Soc.* 2022, 144, 12673−12680
Read Online
ACCESS | Metrics & More | Article Recommendations | Supporting Information

ABSTRACT: The conversion of CO_2 into value-added products is a compelling way of storing energy derived from intermittent renewable sources and can bring us closer to a closed-loop anthropogenic carbon cycle. The ability to synthesize nanocrystals of well-defined structure and composition has invigorated catalysis science with the promise of nanocrystals that selectively express the most favorable sites for efficient catalysis. The performance of nanocrystal catalysts for the CO_2 reduction reaction (CO_2RR) is typically evaluated with nanocrystal ensembles, which returns an averaged system-level response of complex catalyst-modified electrodes with each nanocrystal likely contributing a different (unknown) amount. Measurements at single nanocrystals, taken in the context of statistical analysis of a population, and comparison to macroscale measurements are necessary to untangle the complexity of the ever-present heterogeneity in nanocrystal catalysts, achieve true structure−property correlation, and potentially identify nanocrystals with outlier performance. Here, we employ environment-controlled scanning electrochemical cell microscopy to isolate and investigate the electrocatalytic CO_2RR response of individual facet-defined gold nanocrystals. Using correlative microscopy approaches, we conclusively demonstrate that {110}-terminated gold rhombohedra possess superior activity and selectivity for CO_2RR compared with {111}-terminated octahedra and high-index {310}-terminated truncated ditetragonal prisms, especially at low overpotentials where electrode kinetics is anticipated to dominate the current response. The methodology framework described here could inform future studies of complex electrocatalytic processes through correlative single-entity and macroscale measurement techniques.

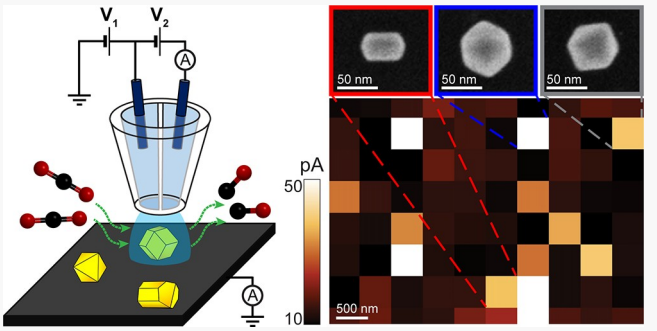

INTRODUCTION

The conversion of CO_2 into value-added chemicals is compelling for storing energy derived from intermittent renewable sources.[1−4] The CO_2 reduction reaction (CO_2RR) is usually associated with large kinetic barriers.[5] The situation is complicated by the competing hydrogen evolution reaction (HER) and similar thermodynamic driving forces for multiple reaction products that could lead to poor product selectivity.[3,5] The ability to synthesize nanocrystals of defined structure and composition has invigorated catalysis science with the promise of nanocrystals that selectively express the most favorable sites for efficient catalysis.[6−17] The electrocatalytic performance of nanocrystal catalysts is typically evaluated with macroscale voltammetric techniques, which returns an averaged system-level response of complex catalyst-modified electrodes.[18] With this approach, identifying features that account for performance can be elusive. The difficulty arises because nanocrystals often present a variety of active sites (e.g., edges, planes, and defects) and their distribution will vary from one nanocrystal to the next even in highest-quality samples.[19]

To realize the knowledge-guided design of next-generation CO_2RR electrocatalysts with superior activity, selectivity, and durability, the measurement of intrinsic electrocatalytic parameters at the single-nanocrystal level and comparison with macroelectrode data to establish reliable structure−activity correlations are critical. With such correlations, the impact of extrinsic factors such as electrode morphology, local pH variation, and mass transfer hindrance can be further elucidated.[20−23] Scanning electrochemical cell microscopy (SECCM) is especially adept at achieving single-entity electrochemical measurements.[24−27] SECCM has been used to resolve the spatial heterogeneity of MoS_2[28,29] and

Received: February 21, 2022
Published: July 6, 2022

https://doi.org/10.1021/jacs.2c02001
J. Am. Chem. Soc. 2022, 144, 12673−12680

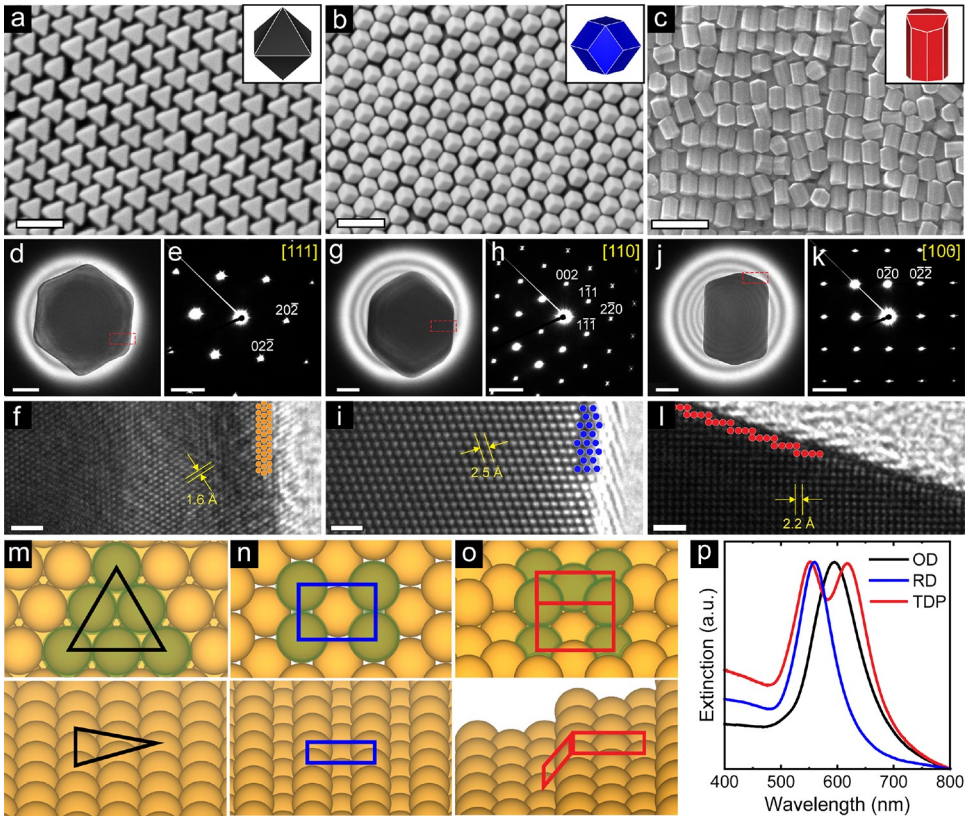

Figure 1. Characterization of facet-defined Au nanocrystal catalysts. (a–c) SEM images and corresponding structural models (insets) of Au (a) OD, (b) RD, and (c) TDP. (d–l) TEM images, coherent nanoarea electron diffraction patterns, and HRTEM images of a single Au (d–f) OD, (g–i) RD, and (j–l) TDP. (m–o) Atomistic models of Au (m) (111)-, (n) (110)-, and (o) (310)-type crystal planes shown in top view (top row) and perspective view (bottom row). Surface unit cells are depicted using colored lines, and the Au atoms regarded as active sites within each unit cell are highlighted with green circles. (p) UV–Vis extinction spectra of different Au nanocrystals. Scale bars: (a–c) 200 nm; (d, g, j) 20 nm, (e, h, k) 5 nm^{-1}, (f, i, l) 1 nm.

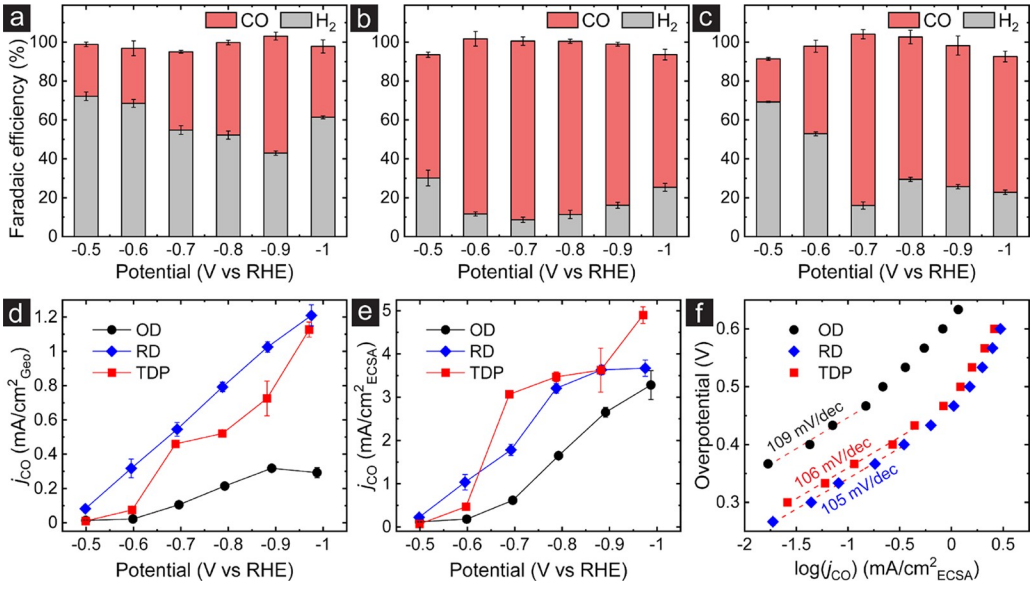

Figure 2. Macroscale CO_2RR performance of Au nanocrystal catalysts. (a–c) Potential-dependent Faradaic efficiencies of CO and H_2 during CO_2RR catalyzed by Au (a) OD, (b) RD, and (c) TDP nanocrystal catalysts. (d, e) CO partial current densities versus cathodic potential normalized by (d) the geometric area of electrode and (e) ECSA. (f) Tafel analysis results of CO_2RR to CO on various Au nanocrystal catalysts. In this work, all potential values are given versus the RHE scale unless otherwise stated.

$Fe_{4.5}Ni_{4.5}S_8$ catalysts[30] for HER and polycrystalline Au catalysts for CO_2RR.[20,22] SECCM has also been used recently to extract kinetic information for oxygen reduction at Pt electrodes[31] and probing oxygen evolution at superparticles[32] and ZIF-derived composites.[33]

https://doi.org/10.1021/jacs.2c02001
J. Am. Chem. Soc. 2022, 144, 12673–12680

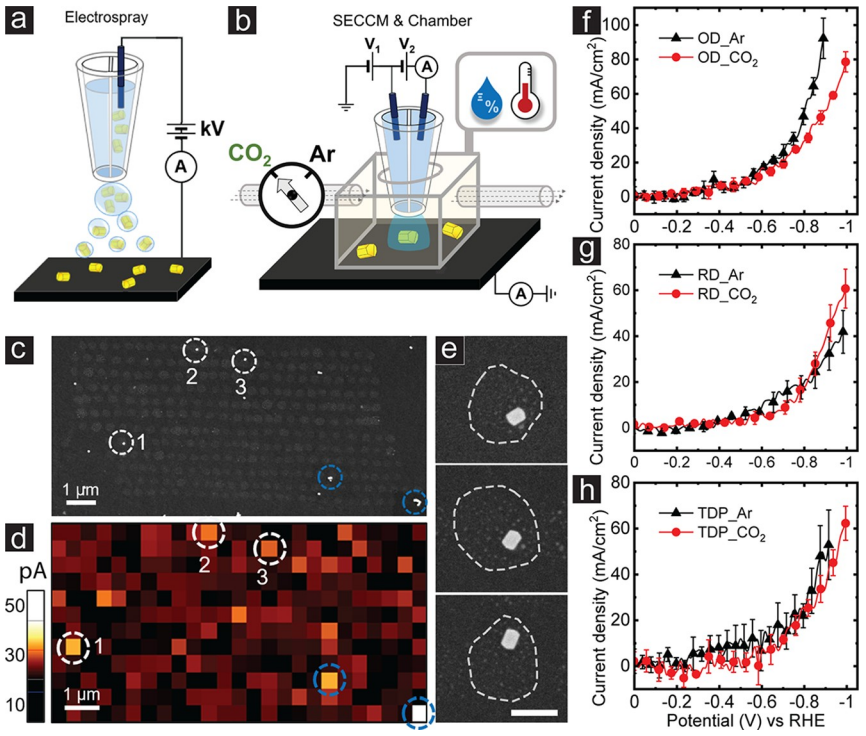

Figure 3. SECCM measurement results of Au CO_2RR catalysts. Schematic depiction of (a) the electrospray setup for Au nanocrystal deposition and (b) environment-controlled SECCM setup. (c) SEM image of Au TDP deposited on GC substrate and (d) corresponding SECCM map at −0.9 V vs RHE under an Ar atmosphere. The scan rate of SECCM LSV was 1.0 V/s. Both isolated Au TDP (white dashed circles) and clusters of TDP (blue dashed circles) are highlighted. (e) High-magnification SEM images of individual Au TDP and electrolyte droplet footprints (white dashed contours) showing fully encapsulated Au nanocrystals during SECCM measurements. Scale bar: 200 nm. (f–h) SECCM LSV results of individual Au (f) OD, (g) RD and (h) TDP under CO_2 and Ar atmosphere. Current densities were calculated using exposed surface areas of nanocrystals measured from SEM images. The error bars were based on data acquired from multiple ($n \geq 3$) isolated nanocrystals. The OD, RD, and TDP samples were deposited onto three separate GC substrates and probed independently with SECCM.

Here, we employ environment-controlled SECCM to isolate and investigate the electrocatalytic response of individual facet-defined Au nanocrystal catalysts for CO_2RR. Au-based materials are among the most active and selective catalysts for electroreduction of CO_2 to CO[5,7,20,22,34−37] and therefore offer a compelling system to study microstructure-dependent catalytic activity and selectivity trends with simple product speciation. With correlative approaches, we conclusively demonstrate that stepped {110} Au facets are more active and selective for CO_2RR than the high-index {310} or close-packed {111} facets. These findings are substantiated by macroscale measurements revealing the average electrocatalytic performance of nanocrystal ensembles.

RESULTS AND DISCUSSION

Single-crystalline Au nanocrystals expressing predominantly one type of crystallographic plane including octahedra (OD), rhombic dodecahedra (RD), and truncated ditetragonal prism(s) (TDP) were synthesized and characterized by electron microscopy (Figure 1a–l and Figures S1–S4). While OD and RD have low-index close-packed {111} and non-close-packed {110} surface facets, respectively, TDP features high-index {310} facets composed of three-atom wide (100) terraces separated by monoatomic steps (Figure 1m–o and Figure S5).[38] Distinctive extinction peaks were observed for these nanocrystals, with TDP displaying two peaks due to shape anisotropy (Figure 1p).

To probe the shape-dependent CO_2RR performance of Au nanocrystals, macroscale electrolysis experiments were conducted (Figures S6–S8) with an equivalent number of nanocrystals deposited on carbon paper electrodes to facilitate comparison (Supporting Information and Table S1). Nanocrystal morphology was well preserved after the removal of surface ligands following our reported procedures (Figure S9).[39,40] Constant-potential electrolysis was conducted to evaluate CO_2RR activity and selectivity (Figure S10) with a CO_2-saturated solution of 25 mM $KHCO_3$ and 10 mM KCl as the electrolyte to better correlate with SECCM studies (see below). Post-mortem SEM images indicated that nanocrystal faceting was well maintained after electrolysis (Figure S11). Figure 2a–c presents CO_2RR product distributions from −0.5 to −1.0 V (vs the reversible hydrogen electrode (RHE) scale). The CO Faradaic efficiency (FE_{CO}) of OD increased monotonically at more negative potentials and reached a peak value of 60% at −0.9 V (Figure 2a). By contrast, a peak FE_{CO} of 88% was attained at −0.7 V for TDP (Figure 2c). Impressively, RD exhibited high FE_{CO} values (exceeding 90%) across a wide potential window from ca. −0.6 to −0.9 V (Figure 2b). The superior CO_2RR performance of RD is also exemplified by its 92% FE_{CO} at −0.6 V, under which the FE_{CO} of OD and TDP was merely 28 and 45%, respectively. To compare the CO_2-to-CO activity among these catalysts, CO partial current densities (j_{CO}) normalized by the geometric area of the electrode are shown in Figure 2d. Au RD exhibited the highest j_{CO} across the entire potential range followed by Au TPD, with Au OD being the least active catalyst. Specific j_{CO}s obtained by normalizing CO partial currents with the electrochemically active surface area (ECSA) were determined

https://doi.org/10.1021/jacs.2c02001
J. Am. Chem. Soc. 2022, 144, 12673−12680

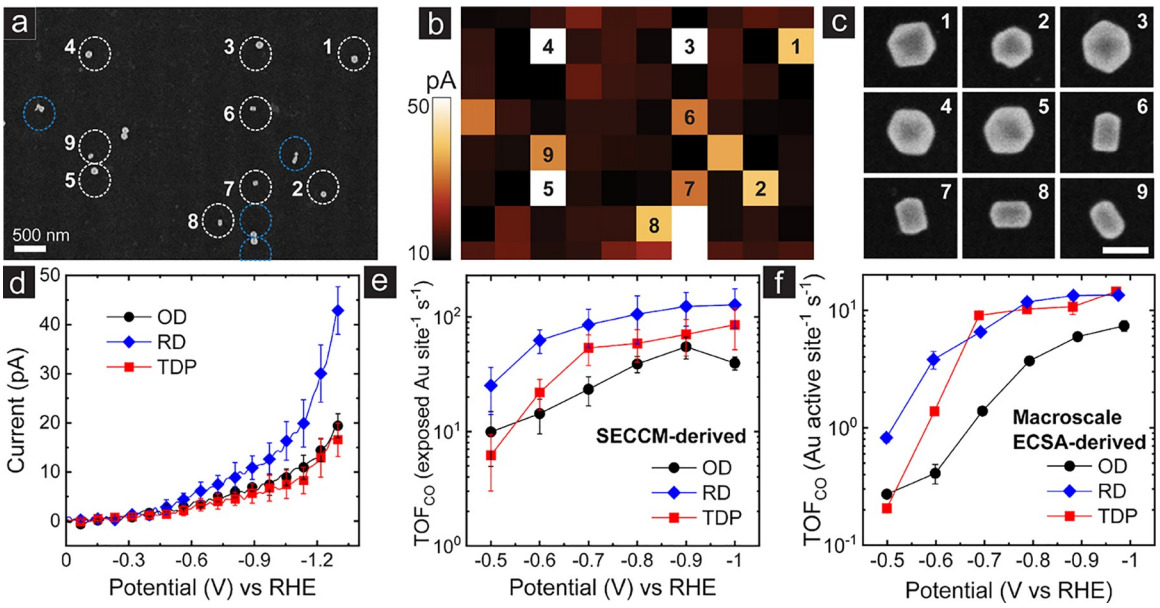

Figure 4. SECCM measurement results and TOF values of individual Au CO_2RR catalysts. (a) SEM image of co-deposited Au RD, TDP, and OD catalysts onto the same GC substrate and (b) corresponding SECCM map at −1.3 V vs RHE under CO_2 atmosphere. The scan rate of SECCM LSV was 1.0 V/s. Both isolated Au nanocrystals (white dashed circles) and nanocrystal clusters (blue dashed circles) are highlighted in (a). (c) High-magnification SEM images of individual Au nanocrystals probed during SECCM mapping. Scale bar: 100 nm. (d) SECCM LSV results of individual Au catalysts under a CO_2 atmosphere. The error bars were based on data acquired from four single-OD, three single-RD, and five single-TDP samples. (e) Potential-dependent TOF_{CO} values obtained by normalizing SECCM-derived CO_2-to-CO partial current densities of a single Au catalyst with the number of exposed surface Au sites calculated based on SEM images of the exact same Au nanocrystal. (f) Potential-dependent TOF_{CO} values obtained by normalizing CO_2-to-CO partial current densities from macroscale measurements with the number of electrochemically active surface Au sites derived from ECSA.

to assess the CO_2-to-CO activity on a per site basis (Figure 2e and Figure S12). OD remained to be the least active catalyst, while TDP appeared to be slightly more active than RD at potentials more negative than −0.6 V. Notably, an opposite trend in activity between RD and TDP was found at low overpotentials (≥−0.6 V), suggesting that RD could be intrinsically more active than TDP in the absence of mass transport limitations (Figure 2e). This interpretation is supported by Tafel analysis results (Figure 2f). The onset overpotential of CO production was 0.27, 0.30, and 0.37 V for RD, TDP, and OD, respectively. A change in Tafel slope at about 0.4 V overpotential was observed for all three catalysts, which likely corresponds to the beginning of mass transfer limits. Tafel slopes extracted from the linear portion of the plots were essentially equal, with 105, 106, and 109 mV/dec for RD, TDP, and OD, respectively. These values are consistent with a mechanistic picture of the initial electron transfer to CO_2 being the rate-determining step, with the caveat that Tafel slope alone is insufficient to verify the CO_2RR reaction pathway.[41] Collectively, our macroscale electrochemical measurements reveal that Au RD have superior CO_2-to-CO activity and selectivity compared with TDP and OD. Previous studies of Au-based catalysts have found that {110} planes possess enhanced CO_2-to-CO activity relative to other low index planes, although whether {110} facets compare favorably with high-index {hk0}-type facets is unclear.[11,34,42,43]

To unravel the structure−function correlations of Au CO_2RR catalysts, electrocatalytic measurements at the single-particle level using SECCM are highly desirable. Despite being straightforward, drop-casting a nanocrystal solution onto a solid substrate often leads to uncontrolled aggregation (Figure S13a). To address this challenge, we have developed an electrospray deposition method that reproducibly affords isolated nanocrystals at modest areal densities (~0.2 particles μm^{-2}), a key prerequisite for single-entity characterization with SECCM (Figure 3a and Figure S13b).[44] Figure 3b shows a schematic of our environment-controlled SECCM setup. A dual-barrel theta pipette filled with 25 mM $KHCO_3$ and 10 mM KCl was approached to the glassy carbon (GC) electrode at a set of predefined locations (Figure S14). This electrolyte composition provides long-term pipette positional feedback control and a negligible drift of the Ag/AgCl quasi-reference counter electrode (QRCE) potential. A nanoscopic electrochemical cell is formed upon each meniscus landing under a precisely controlled humidity, temperature, and gas atmosphere, and localized voltammetric experiments were performed to generate a hyperspectral dataset (Figures S15 and S16). Also, SECCM provides a gas−electrolyte−catalyst triple-phase boundary that mimics the configuration present at a gas-diffusion electrode.[45−47] For gas-consuming reactions, such as CO_2RR, the flux of gaseous reactants is supplied through rapid diffusion across the air−nanodroplet interface onto a small working electrode area. This allows extremely high mass-transport-limited CO_2RR current densities (>20 A cm^{-2}) to be accessed.[20,22]

Comparison between SECCM current maps and corresponding SEM images reveal clear correlation between high current measurements and catalyst locations. One example is shown in Figure 3c,d for Au TDP. This SECCM map was acquired at −0.9 V vs RHE under an Ar atmosphere where HER would be the predominant reaction in this electrolyte. SEM imaging post-SECCM allowed visualization of the droplet footprints so that aggregated nanocrystals (blue dashed circles

https://doi.org/10.1021/jacs.2c02001
J. Am. Chem. Soc. 2022, 144, 12673−12680

in Figure 3c), misshaped particles, or isolated nanocrystals that were not fully encapsulated by the electrolyte meniscus can be identified and excluded from further analysis (Figure 3e). For each Au shape, nanocrystals were deposited onto glass carbon substrates, and SECCM scans were acquired over multiple isolated nanocrystals under CO_2 or Ar atmospheres. Averaged linear sweep voltammetry (LSV) curves are shown in Figure 3f−h, with data processing detailed in Figures S17−S20. Current densities were obtained based on the geometric surface area of individual nanocrystals determined from SEM images (Figures S21 and S22 and Table S2−S4). For OD and TDP, current densities under a CO_2 atmosphere were either comparable or slightly below those under Ar, which may be caused by the suppression of HER in the presence of CO_2 as shown previously for Au-based catalysts.[20,36,48] By contrast, RD showed higher current densities under CO_2 compared with Ar, suggesting that RD is likely the most active CO_2RR electrocatalyst among the three shapes. Importantly, similar trends in current density were found in macroscale LSV scans using the same electrolyte (Figure S23).

To enable more accurate comparison of CO_2RR activity, Au OD, RD, and TDP were codeposited onto the same GC electrode, subjected to identical surface ligand removal treatment, and analyzed by SECCM with the same pipette probe and environmental conditions (Figure 4a) by recording a cyclic voltammogram (CV) at each pixel. Cathodic currents at nanocrystals switched on at about −0.5 V vs RHE and continued to rise at more negative potentials, whereas pixels corresponding to the bare GC electrode remained homogeneously inactive over the whole potential range (Supplementary Movie S1). A snapshot of the SECCM movie at −1.3 V vs RHE is presented to highlight the contrast (Figure 4b). Compared to voltammograms shown in Figure 3f−h, a narrower distribution in current response was observed for each shape (Figure 4c,d and Figures S24 and S25), likely because of the use of one SECCM probe to examine all nanocrystals. Notably, higher Faradaic currents in the anodic scan of the CV were observed for several nanocrystals (Figure S26). We attribute this phenomenon to the incomplete wetting of nanocrystal by the droplet upon initial meniscus contact. For these nanocrystals, full encapsulation was likely achieved either during or after the cathodic scan, possibly due to a combination of droplet formation, electrowetting,[49,50] and surface heterogeneity of the nanocrystal, which results in droplet expansion. This argument is also supported by the increased but stable ionic currents (indicative of droplet size) between the two QRCEs in the anodic scans (Figure S27). When scanning to more negative potentials (−0.7 V vs −1.4 V), the apparent footprint size increased from ca. 408 to ca. 696 nm (Figure S28 and Table S5). These data suggest that the size of the footprint does not change during the anodic scan because the meniscus reaches a steady state at the most negative potential during the cathodic scan and that the droplet retains the larger area once the surface has been wetted. Thus, anodic current traces were used for the comparison of catalytic activity.

Au RD exhibited the highest total currents among the three catalysts under CO_2 atmosphere (Figure 4d). Based on the estimated number of exposed Au sites of each nanocrystal and CO_2-to-CO Faradaic efficiencies obtained from macroscale measurements (Tables S6 and S7 and Figure 2a−c), we further deduced the turnover frequency of CO (TOF_{CO}), an important figure of merit accounting for the intrinsic activity of CO_2RR electrocatalysts (Figure 4e and Figure S29). SECCM-derived TOF_{CO} indicates that the CO_2RR activity follows the order of RD > TDP > OD over nearly the whole potential range (Figure 4e). The same activity order was found for TOF_{CO} derived from macroscale data at low overpotentials (>−0.7 V vs RHE) (Figure 4f). Furthermore, RD exhibited the lowest TOF_{H_2} derived from either macroscale electrolysis or SECCM analyses, and an essentially reversed activity order of RD < TDP < OD was observed for TOF_{H_2} (Figure S30). Although product distribution cannot be quantified with our SECCM setup, we argue that SECCM-derived TOF values are still meaningful for establishing structure−activity relationships for Au-based CO_2RR nanocrystal catalysts. Importantly, previous studies have shown that Au-catalyzed CO_2RR proceeds with enhanced selectivity toward CO in weakly buffering electrolytes such as the one used here, which suggests that the actual TOF_{CO} values under SECCM may even be higher.[36,51−54] The superior CO_2RR activity of RD compared with OD can be accounted for by the low coordination number (CN) of 7 for atoms on the {110} surfaces.[43,55,56] Prior DFT calculations have shown the binding affinity of the *COOH intermediate on Au increases with reduced surface atom CNs and {110} facets to be more active than {100} or {111} for CO_2RR.[1,7,11,42] The {310} planes are composed of atoms with CNs ranging between 6 and 9 (Figure S5), complicating the prediction of the extent to which low-CN atoms may dominate CO_2RR kinetics in experiments.

SECCM maps show that the current response recorded at multiple nanocrystals varies even when particles appear the same by electron microscopy (Figure S26). This highlights that catalytic activities measured at macroelectrodes average the nanoparticle response, obscuring nuances or variations among particles. Further, SECCM-derived TOF (10^2) is an order of magnitude higher than macroscale derived-TOF (10^1) due to the high current density achieved with SECCM. This allows single-particle measurement of CO_2RR activity free of mass-transfer limitations and establishes an activity trend of RD > TDP > OD, which persists over a wide range of potentials and current densities (Figure 4e,f). Our work underscores the importance of designing shape-controlled CO_2RR nanocrystal electrocatalysts that express high-index or low-index stepped (e.g., {110}-type) facets and the benefits of single-entity measurements of catalytic activity at elevated current densities and negligible transport limitations.

CONCLUSIONS

In summary, we have developed a methodology framework for correlative multi-microscopy investigations of colloidal nanocrystal electrocatalysts utilizing macroscale and single-entity electrochemical measurement techniques. Using facet-defined, single-crystalline Au nanocrystals as a model system, we present the first example of SECCM measurements of individual CO_2RR nanocrystal catalysts. We show that {110}-terminated Au RD offer superior activity (expressed as TOFs) and selectivity for CO_2RR compared with {111}-terminated OD and high-index {310}-terminated TDP, especially at low overpotentials where electrode kinetics is anticipated to dominate the current response. The activity order of CO_2-to-CO reduction among these catalysts was confirmed by single-particle SECCM investigations, which evaluated CO_2RR in the more application-relevant, high-current-density regime. We envisage that environment-

https://doi.org/10.1021/jacs.2c02001
J. Am. Chem. Soc. 2022, 144, 12673−12680

controlled SECCM imaging integrated with local product analysis techniques will have a transformative impact on the future development of high-performance electrocatalysts for CO_2RR and other emerging clean-energy technologies.

■ ASSOCIATED CONTENT

Supporting Information

The Supporting Information is available free of charge at https://pubs.acs.org/doi/10.1021/jacs.2c02001.

Spatially resolved CO_2RR activity of individual Au nanocrystal catalysts (MP4)

Detailed experimental methods; additional macroscale electrochemical measurement results; raw SECCM data; structural details of Au nanocrystals measured by SECCM; Supporting Figures S1−S30; Supporting Tables S1−S7 (PDF)

■ AUTHOR INFORMATION

Corresponding Authors

Lane A. Baker − *Department of Chemistry, Texas A&M University, College Station, Texas 77843, United States;* orcid.org/0000-0001-5127-507X; Phone: +1-979-845-4721; Email: lane.baker@chem.tamu.edu

Xingchen Ye − *Department of Chemistry, Indiana University, Bloomington, Indiana 47405, United States;* orcid.org/0000-0001-6851-2721; Phone: +1-812-855-6011; Email: xingye@indiana.edu

Authors

Soojin Jeong − *Department of Chemistry, Indiana University, Bloomington, Indiana 47405, United States*

Myung-Hoon Choi − *Department of Chemistry, Indiana University, Bloomington, Indiana 47405, United States; Department of Chemistry, Texas A&M University, College Station, Texas 77843, United States*

Gargi S. Jagdale − *Department of Chemistry, Indiana University, Bloomington, Indiana 47405, United States*

Yaxu Zhong − *Department of Chemistry, Indiana University, Bloomington, Indiana 47405, United States*

Natasha P. Siepser − *Department of Chemistry, Indiana University, Bloomington, Indiana 47405, United States*

Yi Wang − *Department of Chemistry, Indiana University, Bloomington, Indiana 47405, United States*

Xun Zhan − *Department of Chemistry, Indiana University, Bloomington, Indiana 47405, United States*

Complete contact information is available at: https://pubs.acs.org/10.1021/jacs.2c02001

Author Contributions

#S.J. and M.-H.C. contributed equally to this work.

Notes

The authors declare no competing financial interest.

■ ACKNOWLEDGMENTS

X.Y. acknowledges support from the US National Science Foundation through award DMR-2102526. L.A.B. acknowledges support from the US National Science Foundation through award CHE-1808133. Park Systems is gratefully acknowledged for use of their SICM system. We thank the Indiana University Nanoscale Characterization Facility and Electron Microscopy Center for access of instrumentation. The FIB-SEM used here was acquired through National Science Foundation Major Research Instrumentation grant CHE-0923064. S.J. thanks the Robert & Marjorie Mann Fellowship from Indiana University.

■ REFERENCES

(1) Liu, M.; Pang, Y.; Zhang, B.; De Luna, P.; Voznyy, O.; Xu, J.; Zheng, X.; Dinh, C. T.; Fan, F.; Cao, C.; de Arquer, F. P. G.; Safaei, T. S.; Mepham, A.; Klinkova, A.; Kumacheva, E.; Filleter, T.; Sinton, D.; Kelley, S. O.; Sargent, E. H. Enhanced Electrocatalytic CO_2 Reduction via Field-Induced Reagent Concentration. *Nature* **2016**, *537*, 382−386.

(2) Jiang, K.; Sandberg, R. B.; Akey, A. J.; Liu, X.; Bell, D. C.; Nørskov, J. K.; Chan, K.; Wang, H. Metal Ion Cycling of Cu Foil for Selective C−C Coupling in Electrochemical CO_2 Reduction. *Nat. Catal.* **2018**, *1*, 111−119.

(3) Nitopi, S.; Bertheussen, E.; Scott, S. B.; Liu, X.; Engstfeld, A. K.; Horch, S.; Seger, B.; Stephens, I. E. L.; Chan, K.; Hahn, C.; Nørskov, J. K.; Jaramillo, T. F.; Chorkendorff, I. Progress and Perspectives of Electrochemical CO_2 Reduction on Copper in Aqueous Electrolyte. *Chem. Rev.* **2019**, *119*, 7610−7672.

(4) Verma, S.; Lu, S.; Kenis, P. J. A. Co-Electrolysis of CO_2 and Glycerol as a Pathway to Carbon Chemicals with Improved Technoeconomics Due to Low Electricity Consumption. *Nat. Energy* **2019**, *4*, 466−474.

(5) Hori, Y. I. Electrochemical CO_2 Reduction on Metal Electrodes. In *Modern Aspects of Electrochemistry*; Vayenas, C. G., White, R. E., Gamboa-Aldeco, M. E., Eds.; Springer: New York, NY, 2008; pp 89−189.

(6) Popczun, E. J.; McKone, J. R.; Read, C. G.; Biacchi, A. J.; Wiltrout, A. M.; Lewis, N. S.; Schaak, R. E. Nanostructured Nickel Phosphide as an Electrocatalyst for the Hydrogen Evolution Reaction. *J. Am. Chem. Soc.* **2013**, *135*, 9267−9270.

(7) Zhu, W.; Michalsky, R.; Metin, Ö.; Lv, H.; Guo, S.; Wright, C. J.; Sun, X.; Peterson, A. A.; Sun, S. Monodisperse Au Nanoparticles for Selective Electrocatalytic Reduction of CO_2 to CO. *J. Am. Chem. Soc.* **2013**, *135*, 16833−16836.

(8) Chen, C.; Kang, Y.; Huo, Z.; Zhu, Z.; Huang, W.; Xin, H. L.; Snyder, J. D.; Li, D.; Herron, J. A.; Mavrikakis, M.; Chi, M.; More, K. L.; Li, Y.; Markovic, N. M.; Somorjai, G. A.; Yang, P.; Stamenkovic, V. R. Highly Crystalline Multimetallic Nanoframes with Three-Dimensional Electrocatalytic Surfaces. *Science* **2014**, *343*, 1339−1343.

(9) Reske, R.; Mistry, H.; Behafarid, F.; Roldan Cuenya, B.; Strasser, P. Particle Size Effects in the Catalytic Electroreduction of CO_2 on Cu Nanoparticles. *J. Am. Chem. Soc.* **2014**, *136*, 6978−6986.

(10) Zhu, W.; Zhang, Y. J.; Zhang, H.; Lv, H.; Li, Q.; Michalsky, R.; Peterson, A. A.; Sun, S. Active and Selective Conversion of CO_2 to CO on Ultrathin Au Nanowires. *J. Am. Chem. Soc.* **2014**, *136*, 16132−16135.

(11) Back, S.; Yeom, M. S.; Jung, Y. Active Sites of Au and Ag Nanoparticle Catalysts for CO_2 Electroreduction to CO. *ACS Catal.* **2015**, *5*, 5089−5096.

(12) Luc, W.; Fu, X.; Shi, J.; Lv, J.-J.; Jouny, M.; Ko, B. H.; Xu, Y.; Tu, Q.; Hu, X.; Wu, J.; Yue, Q.; Liu, Y.; Jiao, F.; Kang, Y. Two-Dimensional Copper Nanosheets for Electrochemical Reduction of Carbon Monoxide to Acetate. *Nat. Catal.* **2019**, *2*, 423−430.

(13) Wang, Y.; Cao, L.; Libretto, N. J.; Li, X.; Li, C.; Wan, Y.; He, C.; Lee, J.; Gregg, J.; Zong, H.; Su, D.; Miller, J. T.; Mueller, T.; Wang, C. Ensemble Effect in Bimetallic Electrocatalysts for CO_2 Reduction. *J. Am. Chem. Soc.* **2019**, *141*, 16635−16642.

(14) Huang, J.; Mensi, M.; Oveisi, E.; Mantella, V.; Buonsanti, R. Structural Sensitivities in Bimetallic Catalysts for Electrochemical CO_2 Reduction Revealed by Ag-Cu Nanodimers. *J. Am. Chem. Soc.* **2019**, *141*, 2490−2499.

(15) Shi, Y.; Lyu, Z.; Zhao, M.; Chen, R.; Nguyen, Q. N.; Xia, Y. Noble-Metal Nanocrystals with Controlled Shapes for Catalytic and Electrocatalytic Applications. *Chem. Rev.* **2020**, *121*, 649−735.

(16) Kimura, K. W.; Casebolt, R.; Cimada DaSilva, J.; Kauffman, E.; Kim, J.; Dunbar, T. A.; Pollock, C. J.; Suntivich, J.; Hanrath, T.

Selective Electrochemical CO_2 Reduction During Pulsed Potential Stems from Dynamic Interface. *ACS Catal.* **2020**, *10*, 8632−8639.
(17) Lyu, Z.; Zhu, S.; Xu, L.; Chen, Z.; Zhang, Y.; Xie, M.; Li, T.; Zhou, S.; Liu, J.; Chi, M.; Shao, M.; Mavrikakis, M.; Xia, Y. Kinetically Controlled Synthesis of Pd-Cu Janus Nanocrystals with Enriched Surface Structures and Enhanced Catalytic Activities toward CO_2 Reduction. *J. Am. Chem. Soc.* **2021**, *143*, 149−162.
(18) Kleijn, S. E. F.; Lai, S. C. S.; Koper, M. T. M.; Unwin, P. R. Electrochemistry of Nanoparticles. *Angew. Chem., Int. Ed.* **2014**, *53*, 3558−3586.
(19) Vogt, C.; Weckhuysen, B. M. The Concept of Active Site in Heterogeneous Catalysis. *Nat. Rev. Chem.* **2022**, *6*, 89−111.
(20) Mariano, R. G.; McKelvey, K.; White, H. S.; Kanan, M. W. Selective Increase in CO_2 Electroreduction Activity at Grain-Boundary Surface Terminations. *Science* **2017**, *358*, 1187−1192.
(21) Baker, L. A. Perspective and Prospectus on Single-Entity Electrochemistry. *J. Am. Chem. Soc.* **2018**, *140*, 15549−15559.
(22) Mariano, R. G.; Kang, M.; Wahab, O. J.; McPherson, I. J.; Rabinowitz, J. A.; Unwin, P. R.; Kanan, M. W. Microstructural Origin of Locally Enhanced CO_2 Electroreduction Activity on Gold. *Nat. Mater.* **2021**, *20*, 1000−1006.
(23) Huang, K.; Shin, K.; Henkelman, G.; Crooks, R. M. Correlating Surface Structures and Electrochemical Activity Using Shape-Controlled Single-Pt Nanoparticles. *ACS Nano* **2021**, *15*, 17926−17937.
(24) Ebejer, N.; Schnippering, M.; Colburn, A. W.; Edwards, M. A.; Unwin, P. R. Localized High Resolution Electrochemistry and Multifunctional Imaging: Scanning Electrochemical Cell Microscopy. *Anal. Chem.* **2010**, *82*, 9141−9145.
(25) Snowden, M. E.; Güell, A. G.; Lai, S. C. S.; McKelvey, K.; Ebejer, N.; O'Connell, M. A.; Colburn, A. W.; Unwin, P. R. Scanning Electrochemical Cell Microscopy: Theory and Experiment for Quantitative High Resolution Spatially-Resolved Voltammetry and Simultaneous Ion-Conductance Measurements. *Anal. Chem.* **2012**, *84*, 2483−2491.
(26) Walmsley, J. D.; Hill, J. W.; Saha, P.; Hill, C. M. Probing Electrocatalytic CO_2 Reduction at Individual Cu Nanostructures via Optically Targeted Electrochemical Cell Microscopy. *J. Anal. Test.* **2019**, *3*, 140−149.
(27) Siepser, N. P.; Choi, M.-H.; Alden, S. E.; Baker, L. A. Single-Entity Electrocatalysis at Electrode Ensembles Prepared by Template Synthesis. *J. Electrochem. Soc.* **2021**, *168*, 126526.
(28) Bentley, C. L.; Kang, M.; Maddar, F. M.; Li, F.; Walker, M.; Zhang, J.; Unwin, P. R. Electrochemical Maps and Movies of the Hydrogen Evolution Reaction on Natural Crystals of Molybdenite (MoS_2): Basal vs Edge Plane Activity. *Chem. Sci.* **2017**, *8*, 6583−6593.
(29) Takahashi, Y.; Kobayashi, Y.; Wang, Z.; Ito, Y.; Ota, M.; Ida, H.; Kumatani, A.; Miyazawa, K.; Fujita, T.; Shiku, H.; Korchev, Y. E.; Miyata, Y.; Fukuma, T.; Chen, M.; Matsue, T. High-Resolution Electrochemical Mapping of the Hydrogen Evolution Reaction on Transition-Metal Dichalcogenide Nanosheets. *Angew. Chem., Int. Ed.* **2020**, *59*, 3601−3608.
(30) Bentley, C. L.; Andronescu, C.; Smialkowski, M.; Kang, M.; Tarnev, T.; Marler, B.; Unwin, P. R.; Apfel, U.-P.; Schuhmann, W. Local Surface Structure and Composition Control the Hydrogen Evolution Reaction on Iron Nickel Sulfides. *Angew. Chem., Int. Ed.* **2018**, *57*, 4093−4097.
(31) Chen, C.-H.; Meadows, K. E.; Cuharuc, A.; Lai, S. C. S.; Unwin, P. R. High Resolution Mapping of Oxygen Reduction Reaction Kinetics at Polycrystalline Platinum Electrodes. *Phys. Chem. Chem. Phys.* **2014**, *16*, 18545−18552.
(32) Lu, X.; Li, M.; Peng, Y.; Xi, X.; Li, M.; Chen, Q.; Dong, A. Direct Probing of the Oxygen Evolution Reaction at Single $NiFe_2O_4$ Nanocrystal Superparticles with Tunable Structures. *J. Am. Chem. Soc.* **2021**, *143*, 16925−16929.
(33) Tarnev, T.; Aiyappa, H. B.; Botz, A.; Erichsen, T.; Ernst, A.; Andronescu, C.; Schuhmann, W. Scanning Electrochemical Cell Microscopy Investigation of Single ZIF-Derived Nanocomposite Particles as Electrocatalysts for Oxygen Evolution in Alkaline Media. *Angew. Chem., Int. Ed.* **2019**, *58*, 14265−14269.
(34) Lee, H.-E.; Yang, K. D.; Yoon, S. M.; Ahn, H.-Y.; Lee, Y. Y.; Chang, H.; Jeong, D. H.; Lee, Y.-S.; Kim, M. Y.; Nam, K. T. Concave Rhombic Dodecahedral Au Nanocatalyst with Multiple High-Index Facets for CO_2 Reduction. *ACS Nano* **2015**, *9*, 8384−8393.
(35) Cao, Z.; Kim, D.; Hong, D.; Yu, Y.; Xu, J.; Lin, S.; Wen, X.; Nichols, E. M.; Jeong, K.; Reimer, J. A.; Yang, P.; Chang, C. J. A Molecular Surface Functionalization Approach to Tuning Nanoparticle Electrocatalysts for Carbon Dioxide Reduction. *J. Am. Chem. Soc.* **2016**, *138*, 8120−8125.
(36) Wuttig, A.; Yaguchi, M.; Motobayashi, K.; Osawa, M.; Surendranath, Y. Inhibited Proton Transfer Enhances Au-Catalyzed CO_2-to-Fuels Selectivity. *Proc. Natl. Acad. Sci. U. S. A.* **2016**, *113*, E4585−E4593.
(37) Goyal, A.; Marcandalli, G.; Mints, V. A.; Koper, M. T. M. Competition between CO_2 Reduction and Hydrogen Evolution on a Gold Electrode under Well-Defined Mass Transport Conditions. *J. Am. Chem. Soc.* **2020**, *142*, 4154−4161.
(38) Ye, X.; Gao, Y.; Chen, J.; Reifsnyder, D. C.; Zheng, C.; Murray, C. B. Seeded Growth of Monodisperse Gold Nanorods Using Bromide-Free Surfactant Mixtures. *Nano Lett.* **2013**, *13*, 2163−2171.
(39) Choi, M.; Siepser, N. P.; Jeong, S.; Wang, Y.; Jagdale, G.; Ye, X.; Baker, L. A. Probing Single-Particle Electrocatalytic Activity at Facet-Controlled Gold Naoncrystals. *Nano Lett.* **2020**, *20*, 1233−1239.
(40) Choi, M.-H.; Jeong, S.; Wang, Y.; Cho, S.-J.; Park, S.-I.; Ye, X.; Baker, L. A. Characterization of Ligand Adsorption at Individual Gold Nanocubes. *Langmuir* **2021**, *37*, 7701−7711.
(41) Dunwell, M.; Luc, W.; Yan, Y.; Jiao, F.; Xu, B. Understanding Surface-Mediated Electrochemical Reactions: CO_2 Reduction and Beyond. *ACS Catal.* **2018**, *8*, 8121−8129.
(42) Back, S.; Yeom, M. S.; Jung, Y. Understanding the Effects of Au Morphology on CO_2 Electrocatalysis. *J. Phys. Chem. C* **2018**, *122*, 4274−4280.
(43) Mezzavilla, S.; Horch, S.; Stephens, I. E. L.; Seger, B.; Chorkendorff, I. Structure Sensitivity in the Electrocatalytic Reduction of CO_2 with Gold Catalysts. *Angew. Chem., Int. Ed.* **2019**, *58*, 3774−3778.
(44) Jagdale, G. S.; Choi, M.-H.; Siepser, N. P.; Jeong, S.; Wang, Y.; Skalla, R. X.; Huang, K.; Ye, X.; Baker, L. A. Electrospray Deposition for Single Nanoparticle Studies. *Anal. Methods* **2021**, *13*, 4105−4113.
(45) Higgins, D.; Hahn, C.; Xiang, C.; Jaramillo, T. F.; Weber, A. Z. Gas-Diffusion Electrodes for Carbon Dioxide Reduction: A New Paradigm. *ACS Energy Lett.* **2018**, *4*, 317−324.
(46) Burdyny, T.; Smith, W. A. CO_2 Reduction on Gas-Diffusion Electrodes and Why Catalytic Performance Must Be Assessed at Commercially-Relevant Conditions. *Energy Environ. Sci.* **2019**, *12*, 1442−1453.
(47) Lu, X.; Zhu, C.; Wu, Z.; Xuan, J.; Francisco, J. S.; Wang, H. In Situ Observation of the pH Gradient near the Gas Diffusion Electrode of CO_2 Reduction in Alkaline Electrolyte. *J. Am. Chem. Soc.* **2020**, *142*, 15438−15444.
(48) Feng, X.; Jiang, K.; Fan, S.; Kanan, M. W. Grain-Boundary-Dependent CO_2 Electroreduction Activity. *J. Am. Chem. Soc.* **2015**, *137*, 4606−4609.
(49) Hengsteler, J.; Mandal, B.; van Nisselroy, C.; Lau, G. P. S.; Schlotter, T.; Zambelli, T.; Momotenko, D. Bringing Electrochemical Three-Dimensional Printing to the Nanoscale. *Nano Lett.* **2021**, *21*, 9093−9101.
(50) Valavanis, D.; Ciocci, P.; Meloni, G. N.; Morris, P.; Lemineur, J.-F.; McPherson, I. J.; Kanoufi, F.; Unwin, P. R. Hybrid Scanning Electrochemical Cell Microscopy-Interference Reflection Microscopy (SECCM-IRM): Tracking Phase Formation on Surfaces in Small Volumes. *Faraday Discuss.* **2022**, *233*, 122−148.
(51) Wuttig, A.; Yoon, Y.; Ryu, J.; Surendranath, Y. Bicarbonate Is Not a General Acid in Au-Catalyzed CO_2 Electroreduction. *J. Am. Chem. Soc.* **2017**, *139*, 17109−17113.

https://doi.org/10.1021/jacs.2c02001
J. Am. Chem. Soc. 2022, 144, 12673−12680

(52) Resasco, J.; Lum, Y.; Clark, E.; Zeledon, J. Z.; Bell, A. T. Effects of Anion Identity and Concentration on Electrochemical Reduction of CO_2. *ChemElectroChem* **2018**, *5*, 1064−1072.
(53) Zhang, B. A.; Ozel, T.; Elias, J. S.; Costentin, C.; Nocera, D. G. Interplay of Homogeneous Reactions, Mass Transport, and Kinetics in Determining Selectivity of the Reduction of CO_2 on Gold Electrodes. *ACS Cent. Sci.* **2019**, *5*, 1097−1105.
(54) Ringe, S.; Morales-Guio, C. G.; Chen, L. D.; Fields, M.; Jaramillo, T. F.; Hahn, C.; Chan, K. Double Layer Charging Driven Carbon Dioxide Adsorption Limits the Rate of Electrochemical Carbon Dioxide Reduction on Gold. *Nat. Commun.* **2020**, *11*, 33.
(55) Calle-Vallejo, F.; Tymoczko, J.; Colic, V.; Vu, Q. H.; Pohl, M. D.; Morgenstern, K.; Loffreda, D.; Sautet, P.; Schuhmann, W.; Bandarenka, A. S. Finding Optimal Surface Sites on Heterogeneous Catalysts by Counting Nearest Neighbors. *Science* **2015**, *350*, 185−189.
(56) Todoroki, N.; Tei, H.; Tsurumaki, H.; Miyakawa, T.; Inoue, T.; Wadayama, T. Surface Atomic Arrangement Dependence of Electrochemical CO_2 Reduction on Gold: Online Electrochemical Mass Spectrometric Study on Low-Index Au(hkl) Surfaces. *ACS Catal.* **2019**, *9*, 1383−1388.

https://doi.org/10.1021/jacs.2c02001
J. Am. Chem. Soc. 2022, 144, 12673−12680